CrossMark

Gabor-based spectral domain automated notch-reject filter for quasi-periodic noise reduction from digital images

D. Chakraborty[1] · M. K. Tarafder[1] · A. Banerjee[1] ·
S. R. Bhadra Chaudhuri[1]

Abstract Well-organized restoration techniques for attenuating the impact of periodic/quasi-periodic noise structures from digital images is one of the significant research fields in modern days. These are encountered in various imagery applications like remote-sensing (satellite, aerial), the digitization of canvas paintings, etc. In this paper, a novel spectral domain algorithm for periodic/quasi-periodic de-noising has been presented where an Automated Notch-Reject Filter (ANRF) is lucratively used to remove unwanted periodic patterns from Gabor-transformed corrupted images. As an initial stage, the Low-Frequency Region (LFR) has been conserved ingeniously by finding squared spectral difference after representing the image spectrum as multiple populations. Thereafter, the contrast of any corrupted image spectrum has been increased using Gabor transform for making the noisy components more prominent. Then, an adaptive exponential thresholding procedure has been applied efficiently for detecting those noisy components. The final stage of our proposed algorithm is to filter out those noisy components properly where a novel adaptive notch-reject filter has been applied along with an automated control of filtering profile in proportion to different noise spectrum profile. The supremacy of our algorithm over other state-of-the-art algorithms has been productively established with the help of experimental results in terms of visual and statistical metrics.

✉ D. Chakraborty
  debolina.chk@gmail.com

  A. Banerjee
  ayan@telecom.becs.ac.in

  S. R. Bhadra Chaudhuri
  prof.srbc@ieee.org

[1] ETC, IIEST, Howrah, India

 Springer

1 Introduction

The research area, concerning to the restoration of digital images, corrupted with different types of periodic/quasi-periodic noise patterns has immense significance in various imaging fields [33, 42] since 1940 and was first introduced in [15].

Periodic/quasi-periodic noises may arise from thermal/electrical/electromechanical interferences [11] during image acquisition/transmission and also from electronic interferences like electronic circuitry of the modern digital camera like Charge Coupled Device (CCD) or Complementary Metal Oxide Semiconductor (CMOS) sensors etc. Periodic noises are generally categorized [5] as global, local and striping. Striping pattern [7] may generally occur due to the sensitivity mismatch of the detectors in a multi-imaging system. Another type of periodic noise pattern, known as *Moiré* [30], may often be generated from the entity itself with some periodic patterns having small-scale details near the resolution limit of any digital sensor. Faulty resolution of any scanner, scanning procedure of an electro-optical scanner and an imaging system placed on vibrating holders (aircraft, helicopters, etc) or any moving platforms may also likely to cause this phenomenon [40]. These kinds of noises are most commonly visible in various real-time imagery applications such as medical [19, 23], microscopic [12], remote sensing [6, 20, 31], television [32], planetary mission [29], halftone, raster scanline, canvas contamination in painting artwork [8] etc.

Periodic noises are often represented by the unintended and the spurious repetitive patterns, covering the entire image in the spatial domain. Conversely, these are by nature well-localized in the corresponding Fourier domain image spectrum. To remove periodic noise [26] structures from corrupted images efficiently, though the spatial domain filtering techniques confront several troubles (blurred outputs/artifacts, etc.) due to its spatial dependency all over the image, there are many spatial filters in the literature [17, 18]. On the contrary, noisy spectral components can easily be notified by the Fourier domain based operations as periodic noises confer spiky-peaks/star-shaped peak areas [14] in the corresponding image spectrum, thereby providing superior restoration of the highly corrupted images.

A fundamental frequency and its corresponding harmonics [34] are responsible to create a periodic noise pattern. Ideally, one single-frequency periodic noise can usually cause two sharp spiky-peaks in the image spectrum with almost zero-bandwidth. The presence of several fundamental frequencies, forming such quasi-periodic [13] patterns which is especially visible in most of the non-synthetic dataset. At this point, it is worth mentioning that according to the Gonzalez and Woods [14] also, the existence of numerous star-like zones in any corrupted image spectrum designates the occurrence of more than one sinusoidal pattern i.e. a specific noise structure gets constructed due to the multiple fundamental frequencies. Sharp truncation of any periodic pattern by an image periphery may usually generate different shaped noisy peak areas along with some non-zero bandwidth in the corresponding corrupted image spectrum, depending on the orientation of that repeating pattern.

2 State-of-the-art approaches and their comparative study

Earlier filtering approaches in the spectral domain incorporate some suitable band-selective filters like band-reject, notch-reject, etc. [25] for de-noising images, contaminated by periodic noise patterns. Appropriate determination of noise affected zones centred on their fundamental peaks is quite tricky in these filters. The Procedure for

detecting periodic noise frequencies is resolved to some extent in the spectral domain MFSD1 [1], MFSD2 [2] and WGNF [3].

In Mean Filter in Spectral Domain (MFSD1) [1] method, a ratio of the considered spectral components to the local masked mean value within a sliding and binary window is analyzed with respect to a prefixed threshold value to check whether that spectral component is noisy/ non-noisy. In case of Median Filter in Spectral Domain (MFSD2) [2] approach, a noisy component gets detected if the ratio of the spectral component under concern to the local masked median within a scanning local window exceeds a hand-tuned threshold value. Both MFSD1 and MFSD2 fail to achieve good restoration if the bandwidth of any periodic noise increases. Early selection of two hand-tuned parameters such as threshold and filtering window size by trial and error is cumbersome in these methods. Though computational complexity is comparatively higher, MFSD2 is able to achieve a little bit better performances than MFSD1 especially in case of quasi-periodic noise structures.

A semi-automatic process for periodic denoising was proposed by Hudhud and Turner [16]. Immediately, after the detection of noisy peaks, square/elliptical shaped Region of Interest (ROI) was determined. Then, those were filtered out using a weighted median filter. Though the time complexity is slightly improved there by using ROI, still this filter suffers from the similar problem as in the paper [2]. The Spike estimation process is not clearly described by them as well as ROI determination is not at all automatic.

In the paper [3], an efficient semi-adaptive method, i.e. Windowed Gaussian Notch Filter (WGNF) for periodic/quasi-periodic noise detection and filtration was demonstrated. In this approach, noisy peaks were detected using a similar process as in the paper [2] and then filtered out by a modified version of the ideal *Gaussian notch-reject filter* [14]. Due to the usage of fixed window size and prefixed coefficients of this filter, this procedure is also not capable of producing good restoration with upto the mark.

A pioneering semi-automatic software solution [22] in the spectral domain was suggested for attenuating noisy peaks from dual energy images (*such as X-ray mammography*) using two regions cross-shaped *top-hat* filters like Interpolation Notch-Reject Filter (INRF), Brickwall Notch-Reject Filter (BNRF) and Gaussian Notch-Reject Filter (GNRF). The authors used such fixed thresholding approach which may perform satisfactorily for a few special cases only. Central $4 * 4$ fixed region was protected by them for restoring authentic image information even for such natural images which have more dispersed central region.

A suitable notch-pass filter like Adaptive Optimum Notch Filter (AONF) [27] was applied to the input corrupted image spectrum to extract the knowledge of corresponding repetitive pattern in the spatial domain.

Gaussian Star Restoration Filter (GaSF) for periodic/quasi-periodic denoising from digital images was presented in the paper [21]. Two orthogonal and elliptical Gaussian filtering profiles for each noisy peak were utilized by the authors to design a *star-shaped* filter. For designing this GaSF, usage of three kinds of hand-tuned threshold values and a few estimated parameters may lead to a bad restoration.

In VSNR [12], at first, a new class of random process, approximating many real-life stationary noises of numerous fields were proposed. Then the image was restored from the contaminated one using a Bayesian method by interpreting this restoration technique as a convex optimization problem which was solved numerically. The authors decomposed the noise for certain advantages, but fail to handle the random Gaussian part of it. This restoration process is a time consuming iterative procedure, applicable only for the certain types of stripe noises which usually obey one specific hypothesis.

In the paper [28], a novel Adaptive Gaussian Notch Filter (AGNF) was launched as the scheme of reducing the impact of periodic noises efficiently. As compared to the rest other existing methods, AGNF does not require any tuning and parameter adjustments. The procedure for detecting LFR is not optimum and fit for every scenario in case of AGNF [28]. Also, it uses a fixed Gaussian filtering profile irrespective of the filtering window size.

The authors [6] presented a process of de-striping of the multispectral remote sensing images. They preserved spectral and spatial consistency of images by categorizing the stripes and then removed the same by utilizing 3D total variation. They used the Split-Bregman iteration for fast optimization of the de-striping model. They assumed that the image feature gradient must be lesser than the stripe gradient. If it fails then there is a chance of losing the edge information of the original image. As this technique is based on the optimization, the iterative process demands more execution time.

Sur, Grediac [36] established an automated approach of removing quasi-periodic noise structures from natural images. At first, a robust regression analysis was employed by fitting the power-law to the input corrupted image power spectrum to get a flavour of expected noise-free natural image power spectrum. The expected power spectrum was then compared with the average power spectrum obtained from the set of regularly distributed patches to localize noisy peaks. Finally, they applied an automated notch-reject filter to detect the method noise which was eventually eradicated from the corrupted image in the spatial domain.

In the paper [35], the concept of Number of False Alarm (NFA) was exploited over the uniform concentric rings to detect spurious noisy peaks. Minimum of power spectrum was utilized to perform the same. It takes a large amount of execution time due to NFA calculation. Both the works [35, 36] experience the fixed patch size problem, thus may not give the best result for every image-noise combinations. As both of them follow a non-adaptive LFR detection procedure, their performance for low-frequency noise removal is not at all acceptable.

The authors of the work Laplacian based Frequency Domain Filter (LFDF) [38] divided the entire algorithm into two major stages: noisy component detection and correction. At first, noisy regions were highlighted by convolving the corrupted image spectrum with the *Laplacian directional mask*. Then, noisy peaks were found out by comparing each spectral component with a non-adaptive threshold value which was a function of *Euclidian distance* from the DC element. Finally, those noisy components were recursively restored using the average of minimum and median values of nearest possible uncorrupted components.

Windowed Adaptive Switching Minimum Filter (WASMF) [39] is a slightly modified version of LFDF [38]. They detected noisy peaks using such a thresholding approach which differs from LFDF but still depends on the *Euclidean distance* from DC element. Once a peak had been identified, the associated noisy areas were then recognized by comparing with another threshold value which was dependent on local neighbourhood statistics. In the noise attenuation phase, detected noisy frequencies were recursively replaced by the minimum value of uncorrupted frequencies within a local neighbourhood. LFDF and WASMF used such fixed thresholding approach which is not a function of the corrupted image itself. So, these procedures cannot perform optimally for a large span of image-noise combinations. In both LFDF and WASMF, time consumption is more than the notch filtering one due to the recursive filtering procedure.

A recent technique of periodic/quasi-periodic noise fading i.e. Adaptive Threshold based Frequency Domain Filter (ATFF) is well described in the paper [37]. As a pre-processing step, they used *Laplacian transform* as described in [38] to make the corrupted image spectrum more prominent, thereby suggesting an adaptive threshold based noise identification process.

Hence, corrupted frequencies were attenuated using the minimum filter as in [39]. Their peak detection method becomes uncertain unless the multiplicative parameter, used during thresholding, gets optimized.

This paper presents a fully automated frequency domain denoising algorithm for digital images, impaired by a wide range of periodic/quasi-periodic noise patterns by alleviating the inadequacy of other existing frequency domain algorithms. It is capable of discriminating noisy frequencies from the non-noisy ones effectively since it has the unique ability to separately identify the noisy fundamental peak and its surrounding noisy affected areas. Novelty of our proposed *Gabor-based ANRF* algorithm is bestowed at our level best utilising some well-known mathematical theories or our own innovated procedures in each of its several distinct steps (Fig. 1). To start with, our algorithm preserves entire LFR, containing smooth image information, precisely by representing the whole image spectrum as multiple populations where each population consists of several spectral components. Here, *squared spectral difference* of each spectral component of every population with respect to the median of the considered population is utilised for LFR conservation. Thereafter, detecting the effective noisy spectral zone easily, remaining image spectrum gets highlighted more prominently by using *Gabor transform* which is the maiden usage so far. Though the idea of highlighting the whole image spectrum is
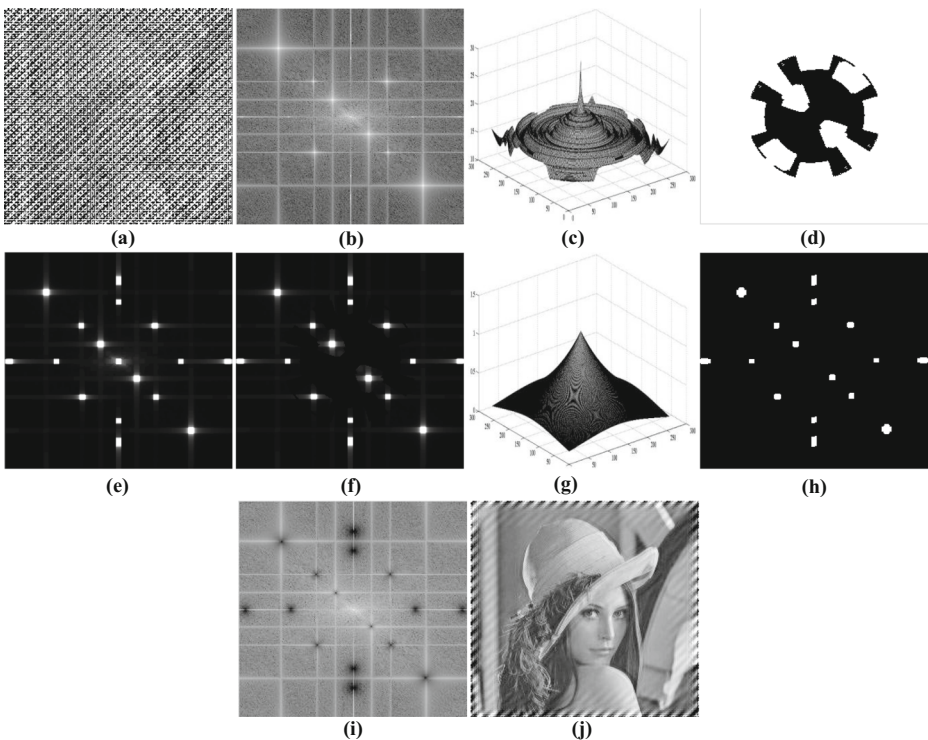

Fig. 1 Propostion of Gabor-based ANRF Algorithm. Pictorial representation of the stages of our proposed algorithm: **a** Standard image Lena, synthetically contaminated by combined noise $(N_1 + N_2 + N_3)$ as in Eq. 27 with $A = 0.7$; **b** Corrupted image spectrum; **c** 3D plot of expected model of noise-free natural image; **d** LFR mask with widened radius and angle; **e** Contrast enhanced spectrum using Gabor Transform; **f** LFR Masked Gabor Transformed Spectrum; **g** 3D plot of Threshold Surface; **h** Noisy Bitmap; **i** Restored image spectrum; **j** Restored image

acquired from some of the latest existing works [37–39], their implementation approach differs from us to a great extent. To perform the same, the works of [37–39] used inherently inflexible *Laplacian kernel* as a pre-processing step before LFR preservation whereas a more flexible Gabor profile is employed in our case after LFR preservation. Unlike our work, the complexity of those works is greatly increased as the contrast enhancement step is executed before preserving LFR contents. In accordance with this step, the parameters involved in their subsequent steps must be adjusted vigorously if there is a requirement of modifying *Laplacian kernel* of [37–39] to highlight the spectrum for certain image noise combinations which may introduce extensive calculations. In our case, after using a well-customised *Gabor profile* to make it more suitable for varying image-noise combinations, an adaptively calculated novel threshold surface using an exponential function is exploited to get the noisy bitmap. At last, a novel *automated notch-reject filter* is proposed by us with an automated control of filtering profile in accordance with the largest radial span of differently shaped noise spectrum profiles to attenuate the effective noisy peak areas.

3 Proposition of Gabor-based ANRF algorithm

To start with, *IM* of size $R * C$ is considered here as the origin shifted *Fourier transformed* spectral domain representation of an image, corrupted with various kinds of periodic/quasi-periodic noise patterns. It is noteworthy to mention that the position of any pixel/spectral component of an image matrix can usually be represented by several conventions as given below.

1. In the Cartesian method, (x, y) or (u, v) represents the corresponding row and column position in the spatial/spectral domain respectively.
2. In Polar method, (r, θ) represents the radius from the DC element and the angular displacement from the positive horizontal axis that passes through DC and
3. In single indexing method, i indicates the positional representation of an element in any image matrix while row/column traversing.

One of the abovementioned specific methods for such representations can easily be transferred to other by some simple numerical analysis. Hence, these representations are utilized in this article for making our mathematical expressions more convenient.

3.1 Entire LFR preservation using mask formation

At this juncture, Power Spectrum of Corrupted Image (PIM) is regarded as a set of concentric rings, centered on the DC value of *IM*. Naturally, each of the rings corresponds to a *population/collection* of the power of spectral components of any corrupted image. So, as a whole *PIM* can be considered as a combination of several populations i.e. *PL* where each population (pl^j, where j is the positional index of *PL*) contains the power of the spectral components, known as *sample*. In this sub-section, our main motto is to preserve LFR appropriately in an automated way by applying a rough thresholding to detect the outliers. Outliers of each population are detected using a rough threshold value (τ) by finding the *squared spectral difference* between

each sample of the jth no. population and the median of that corresponding population. As LFR span cannot usually be exceeded by half of the Maximum Possible Radius (M_R), the total number of population must be limited by this.

$$OUTLIER = \bigcup_{j=1}^{M_R/2} (r, \theta)^j, if \left[pl_{r,\theta}^j - Median\left(pl^j\right)\right]^2 > \tau^j \qquad (1)$$

Where, $\tau^j = \frac{\left[Mean\left(pl^j\right) + Median\left(pl^j\right)\right]}{2}$, $pl^j \in PL$ and $(r, \theta)^j$ represents the collection of positions of samples within the jth no. population. The procedure for finding Outlier Bitmap (OB) is mathematically outlined in the following:

$$OB = \begin{cases} 1, \forall (r, \theta) \in & OUTLIER \\ 0, & otherwise \end{cases} \qquad (2)$$

LFR Mask (M) can then be accurately formed with the help of *OB* to keep LFR intact.

$$M = \begin{cases} 1, & if \ o\beta_{r,\theta} = 1 \\ 0, & otherwise \end{cases} \qquad (3)$$

Where, $o\beta_{r,\ \theta} \in OB$

After formation of *M*, we update *M* by relaxing the mask a little bit around each and every outlier on bitmap as there may be any noisy affected region which would be detected precisely on the later part of the algorithm. Hence, radius and angle widening are incorporated to perform the same as mathematically explained in Eq. (4a) and Eq. (4b) respectively.

$$M = \left\{ 1, if \ o\beta_{r1,\theta} = 1 \& [r1 < r \ OR \ r1 < r + 5] \right\} \qquad (4a)$$

$$M = \left\{ 1, if \ o\beta_{r,\theta1} = 1 \& \left[\theta - 5° < \theta1 < \theta + 5°\right] \right\} \qquad (4b)$$

Where, $r1$ and $\theta1$ are temporary variables, indicating values of r and θ.

3.2 Adaptive thresholding using exponential surface

Suitable and proper thresholding is the most requisite process of detecting noisy fundamental peaks along with their surrounding noise affected zones. Before applying an adaptive thresholding procedure, at first, *Gabor transform* [9, 10] is applied to *IM* to make the spectrum more prominent which in return leads to a contrast-enhanced version of *IM*, thereby making noisy peaks along with their surrounding zones more distinguishable and clearly visible. Now, it gets much easier to apply threshold surface to identify those noisy peaks along with their noise affected zones. Gabor-Transformed Image Spectrum ($\dot{\mathcal{GS}}$) is found out by convolving $\dot{G}$ with *IM* as outlined in Eq. (5).

$$\dot{GS} = \dot{G} \otimes IM \qquad (5)$$

Where, $\dot{G}$ is a *Gaussian function* modulated by sinusoid, together termed as *Gabor*

$$\dot{G}_{(u,v)} = \frac{1}{2\pi\sigma^2} exp\left(-\frac{u_\phi^2 + \gamma v_\phi^2}{2\sigma^2}\right) * cos\left(\frac{2\pi u_\phi}{\lambda} + \varphi\right) \qquad (6)$$

$u_\phi = u \ cos \ \phi + v \ sin \ \phi$ and $v_\phi = -u \ sin \ \phi + v \ cos \ \phi$

σ, λ, ϕ, γ and φ refer to the standard deviation of $\dot{G}$, wavelength of the sinusoids, orientation of the normal to the parallel stripes of $\dot{G}$, spatial aspect ratio and phase offset respectively. In our case, controlling parameters of $\dot{G}$ are selected as: $\sigma = 1, \lambda = 5, \phi = \frac{\pi}{2}, \gamma = 0.5, \varphi = 0$. As most of those chosen values are conventionally standard assumption, a standard $\dot{G}$ is then obtained. Moreover, all the values of those parameters bear some logical suitability criteria for our case. Any $\dot{G}$ having $\sigma = 1$ is a general assumption as it can cover the whole image quite satisfactorily for a wide range of image sizes. The value of ϕ denotes the angle between horizontal and vertical axes of $\dot{G}$. As the images are usually planar and we need to apply any $\dot{G}$ in a way such that its effect will fall upon the whole images homogeneously, so the value of ϕ is appropriate enough to take as $\pi/2$. Here, the value of the parameter φ is taken as 0 to make the peak of any $\dot{G}$ perfectly aligned with the spectral position of the DC value of the image so as to produce the best result. As any $\dot{G}$ is usually composed of an exponential function along with a sinusoid, we can say that the nature of $\dot{G}$ is similar to exponentially decreasing sinusoidal ripples. Whenever the wavelength of the sinusoid increases, it creates fewer amounts of ripples with low frequency. To get the high contrast enhancement, we would like to have such $\dot{G}$ which contains high-frequency ripples. So, lower value of λ is generally desirable for achieving the high contrast enhancement of an image. Our algorithm is run for a wide range $(1-20)$ of λ for various synthetic/non-synthetically corrupted images. Within this range of λ, the quality of restored images will be good enough in terms of both statistical and visual, thereby achieving best results amongst others. In our case, λ is set at 1 as the smallest suitable value of that wide range of λ. Now, Normalized LFR Masked Gabor Transformed Spectrum (N) is established as given in the following:

$$N = \frac{M \circ \dot{G}\mathcal{S}}{Max\,(M \circ \dot{G}\mathcal{S})} \tag{7}$$

Where, the operator $\circ$ belongs to *Hadamard product* operation. Now, for finding out noisy bitmaps, an appropriate Threshold Surface (Ŧ) has to be created to act upon any *IM* which is generally random in nature. So, the centre of such surface should be perfectly aligned with the position of the DC value of any *IM*. In Eq. (8), a generalized exponential surface is considered as Ŧ, containing two parameters A and S for controlling *Amplitude* and *Slope* of such exponential function based on which Ŧ is created. Amongst many other non-linear functions, the exponential function is preferred in our case as it is always handy because by controlling A and S suitably, we can easily approximate many random data sets.

$$Ŧ = \bigcup_{u=1}^{R} \left\{ \bigcup_{v=1}^{C} A * exp \left[-S * (\sqrt{u^2 + v^2}) \Big/ M_R \right] \right\} \tag{8}$$

In our case, A is signified by the maximum amplitude of N which usually falls after $M_R/2$ upto image boundary as noisy components generally reside after LFR.

$$A = Max\{\nu_{r,\theta}\}\ where, r > (M_R/2) + 1\ and\ \nu_{r,\theta} \in N \tag{9}$$

In Eq. (9), r represents the radial outward distance from the position of DC element and θ denotes angle with respect to the positive horizontal axis that passes through DC. For detecting the value of S, here N is considered as the combination of

closely spaced Radial Vectors (H), containing varying amplitudes of spectral coefficients, i.e. the distributions of different amplitudes. It is mathematically expressed as:

$$H_\theta = \bigcup_{r=1}^{M_R} \eta_{r,\theta} \qquad (10)$$

Where, $0^\circ \le \theta \le 180^\circ$ and $\eta_{r,\theta} \in H$

Here, for determining the appropriate value of S for $Ŧ$, two ultimate Hs i.e. H_{SMax} and H_{SMin} are chosen among all H s based on the maximum and the minimum values of the Standard Deviation (Std). H_{SMax} indicates such a particular H which has the maximum amplitude variation i.e. higher possibility of having noisy frequencies. For H_{SMin}, the scenario is exactly opposite.

$$H_{SMax} = \left\{ H_{\theta 1}, if\ Std(H_{\theta 1}) = Max\left[\bigcup_{\theta=0^\circ}^{\theta=180^\circ} Std(H_\theta) \right] \right\} \qquad (11a)$$

$$H_{SMin} = \left\{ H_{\theta 1}, if\ Std(H_{\theta 1}) = Min\left[\bigcup_{\theta=0^\circ}^{\theta=180^\circ} Std(H_\theta) \right] \right\} \qquad (11b)$$

In Eq. (11a) and (11b), $\theta1$ indicates temporary variable, indicating the values of θ. Now, the random amplitude distributions of H_{SMax} and H_{SMin} are made approximately fit with a suitable exponential function by varying the values of S of that function. Two extreme values of S i.e. S_{Max} and S_{Min} are subsequently calculated so that their corresponding exponential functions can pass through the halfway of the maximum amplitude span of the distributions of H_{SMax} and H_{SMin}.

$$S_{Max} = \left[Min\{S, if\ \textstyle\sum_i \eta_{SMaxi} - A * exp(^{-S*i}/_{M_R}) > 0\} \right]/2 \qquad (12a)$$

$$S_{Min} = \left[Min\{S, if\ \textstyle\sum_i \eta_{SMini} - A * exp(^{-S*i}/_{M_R}) > 0\} \right]/2 \qquad (12b)$$

Where, i is the positional index of the corresponding sets like H_{SMax} and H_{SMin}. Hence, $\eta_{SMaxi} \in H_{SMax}$ and $\eta_{SMini} \in H_{SMin}$. In Eq. (12a) and (12b), after several experimental observations, the range of S is sufficient enough to take as $1 \le S \le 10$. S_{Max} corresponds to that exponential function which approximates the distribution of H_{SMax} having higher possibility of containing noisy peaks. Hence, if we select S_{Max} solely as the value of S for thresholding surface, then all noisy components may not be detected. That's why, S_{Min} and average of S_{Max} and S_{Min} are used as two possible appropriate values of S i.e. S1 and S2 for finding two suitable threshold surfaces i.e. $Ŧ1$ and $Ŧ2$.

$$S1 = S_{Min}\ and\ S2 = \left\lfloor \frac{S_{Max} + S_{Min}}{2} \right\rfloor \qquad (13)$$

At this juncture, in accordance with $S1$ and $S2$, the generalized $Ŧ$ as expressed in Eq. (8) is then customized into $Ŧ1$ and $Ŧ2$ as delineated below:

$$Ŧ1 = \bigcup_{i=1}^{R*C} A * exp \left({-(S1 * i)} / {M_R} \right) \tag{14a}$$

$$Ŧ2 = \bigcup_{i=1}^{R*C} A * exp \left({-(S2 * i)} / {M_R} \right) \tag{14b}$$

In Eq. (14a) and Eq. (14b), variable i denotes the distance of each spectral components' position with respect to the DC value's position of IM.

3.3 Noisy bitmap generation

After applying $Ŧ1$ and $Ŧ2$ to input IM, two Noisy Bitmaps ($ℬ1$ and $ℬ2$) are subsequently obtained which mainly comprise of noisy fundamental peaks surrounded by their effective noisy spectral zones.

$$B1 = \begin{cases} 1, & if \ \eta_i \geq T1_i \\ 0, & otherwise \end{cases} \tag{15a}$$

$$B2 = \begin{cases} 1, & if \ \eta_i \geq T2_i \\ 0, & otherwise \end{cases} \tag{15b}$$

Where, $i \in \{1, (R*C)\} \subset \mathbb{Z}^+$

Now, all the closed contours are detected which actually refer to the different shapes of various noisy spectral zones of the corresponding 1 and 2 respectively. After that, positions of all the spectral components, bounded by each closed contour are stored in Contour Map ($Č$) sequentially. Thereby, positions of the fundamental peaks of all the noisy contours correspond to 1 and 2 are detected, known as Fundamental Peak Positions ($ℙ1$ and $ℙ2$) respectively.

$$P1 = \left\{ j, if \ im_j = Max(im_k), \forall k \in č1_i \ where \ č1_i \in Č1 \right\} \tag{16a}$$

$$P2 = \left\{ j, if \ im_j = Max(im_k), \forall k \in č2_i \ where \ č2_i \in Č2 \right\} \tag{16b}$$

In Eq. (16a) and Eq. (16b), im_j, $im_k \in IM$ and j, k are the positional indexes of the corresponding set IM. Now, we have to determine the Final Contour Map ($FČ$) and the Final Set of Fundamental Peak Positions ($Fℬ$) corresponds to the Final Noisy Bitmap ($Fℬ$) which is much more suitable for a specific image-noise combination. This is highly dependent on the number of noisy peaks detected in $ℙ1$ and $ℙ2$

respectively. So, the difference between Cardinality (Card) of two sets i.e. $\mathcal{P}1$ and $\mathcal{P}2$ is exploited to do the same.

$$Diff = [Card(\mathrm{P}1) - Card(\mathrm{P}2)] \qquad (17)$$

After that, for choosing F, the value of $Diff$ is compared with a suitable function of the difference between $S1$ and $S2$.

$$Diff_{lim} = C1 * (S2 - S1) + 1 \qquad (18)$$

Where, $C1 = 1.5$ is considered typically after the experimental analysis. The decision about the appropriate bitmap is taken as follows,

$$[\mathcal{FP}, \mathcal{FB}, \mathcal{F\check{C}}] = \begin{cases} [\mathcal{P}2, \mathcal{B}2, \check{C}2], & if \ Diff > Diff_{lim} \\ [\mathcal{P}1, \mathcal{B}1, \check{C}1], & Otherwise \end{cases} \qquad (19)$$

It is conferred from the above Eq. (19) that if there is a small difference between $S2$ and $S1$ along with the large values of $Diff$ then we will take that bitmap as appropriate which is corresponding to a larger value of S and vice-versa.

3.4 Automated notch filtration on effective noisy spectral zone

The final and most important step of any denoising algorithm is the *filtering* of any effective noisy spectral zones centred on their fundamental peaks. Here, an Automated Notch-Reject Filter (ANRF) is introduced with an adaptive control of filtering profile (Fig. 2) in accordance with the different shapes of the noise spectrum profiles. This phenomenon makes it superior to most of the existing works where filtering profile is fixed in nature [3, 28]. For managing filtering profile in accordance with an effective
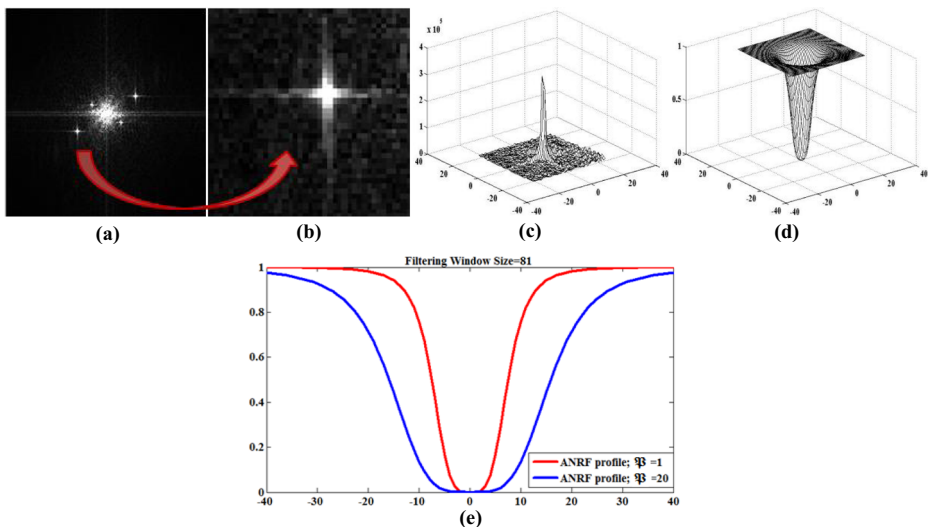

Fig. 2 **a** Spectrum of real image Clown; **b** Close-up view of Noise Frequency in 3rd quadrant; **c** Noise Spectrum Profile; **d** Proposed ANRF profile; **e** 2D Characteristics curve of our proposed ANRF profile for different values of X

noisy spectral zone, the slope of attenuation i.e. nothing but the profile of any filtering surface has to be directly dependent on the maximum radial span of that zone. Hence, a linear relationship of Profile Controlling Parameter (X) of our filtering surface is made with the Largest Radial Distance (Ω) of the ith closed contour of $ƑČ$ centred on the corresponding fundamental peak.

$$X = \bigcup_{i=1}^{Card(ƑČ)} \{C2 * (\omega_i + C2), where\ \omega_i \in \Omega\} \tag{20}$$

Where,

$$\Omega = \bigcup_{i=1}^{Card(ƑČ)} Max\{Ɇ(ƒþ_i, j), where\ ƒþ_i \in ƑP, j \in ƒč_i\ and\ ƒč_i \in ƑČ\}$$

Typically, $C2 = 5$ is regarded as the best-chosen value after various experimental observations and $Ɇ$ represents the *Euclidean distance* in the spectral domain. From Eq. (20), it can be inferred that a high value of X is required to efficiently filter out any noisy spectral zone with large radial span and the scenario is exactly opposite for small radial span. Hence, the characteristics of our proposed filtering profile adapt the slope of attenuation of our filtering surface in accordance with the radial span of any noise spectrum profile.

Generally, the maximum possible span of any noisy spectral zone can be limited by the half of its Nearest Peak Distance (Đ) i.e. minimum $Ɇ$ of any considered peak from its nearest peak/ DC component. Here, half of the $đ_i$ (*where* $đ_i \in Đ$) as the maximum Filtering Profile Window ($W_i * W_i$) is considered to give freedom to the χ_i (*where* $\chi_i \in X$) for controlling the effective filtering profile's roll-off with respect to the span of the noise spectrum profile, referring to the ith noisy peak. Hence, $W_i * W_i$ can cover up the whole noisy spectral zone even in the case of its maximum possible span i.e. $đ_i/_2$. It is indispensible to efficiently restore the uncorrupted spectral components as much as possible by using appropriate value of χ_i for effectively rolling off the filtering profile in relation to the span of the noise spectrum profile, thereby avoiding the chances of unwanted filtering. As the values of i varies from 1 to the cardinality of the set $ƑP$, each corresponding values of $đ_i$ is stored in a set $Đ$. The formation of the set $Đ$ is mathematically expressed as:

$$Đ = \bigcup_{i=1}^{Card(ƑP)} Min \left[Min\{Ɇ(ƒþ_i, ƒþ_j)\}, Ɇ(ƒþ_i)\right], where\ i \neq j\ and\ ƒþ_i, ƒþ_j \in ƑP \tag{21}$$

Where, the single argument in $Ɇ$ specifies the distance of the considered noisy peak from the DC component. Finally, our proposed ANRF of size $W_i * W_i$, used for image restoration is given by,

$$ANRF_{W_i} = \cfrac{1}{1 + \left[\cfrac{\sqrt{2} * \left|\frac{W_i}{2}\right|}{(u_i^2 + v_i^2)}\right]^2 * \chi_i}, for\ -\left|\frac{W_i}{2}\right| \leq (u_i, v_i) \leq \left|\frac{W_i}{2}\right| \tag{22}$$

Where, $W_i = \{đ_i + 1\ where\ đ_i \in Đ\}$ and $\chi_i \in X$

The whole procedure of our proposed ANRF denoising method is recapitulated in a nutshell for making it more realizable using Algorithm 1 as demonstrated below:

Algorithm 1: Procedure of Image Denoising With Gabor-based ANRF Algorithm

Begin,

    Input: Corrupted Image

        Transform input into spectral domain as IM

        Detect outliers: Apply rough threshold $\tau^j = \frac{[Mean(pV) + Median(pV)]}{2}$ on PIM

        Mask the LFR region creating M

        Relaxing M both angle and radius wise by following Eq. 4(a) & Eq. 4(b)

    Creating $\dot{G}\mathcal{S}$ by $\dot{G}\mathcal{S} = \dot{G} \otimes IM$

    Creating N from $\dot{G}\mathcal{S}$ using $N = \frac{M \circ \dot{G}\mathcal{S}}{Max\,(M \circ \dot{G}\mathcal{S})}$

    Evaluate control parameters A and S for Ŧ1 and Ŧ2

    Compute Ŧ1 and Ŧ2

    Generate noisy bitmaps B1 and B2

    Detecting P1 and P2 and then creating a set ₣P

    Compute customized X for each of the noisy peak by

$$X = \bigcup_{i=1}^{card\,(F\dot{C})} \{C2 * (\omega_i + C2); \; \omega_i \in \Omega\}$$

    Fixing the window size $(W_i * W_i)$ around i^{th} noisy peak using $(d_i + 1) * (d_i + 1)$

    Apply final filtering profile on noisy spectral zones centred on their fundamental peaks as

$$ANRF_{W_i} = \frac{1}{1 + \left[\frac{\sqrt{2} * \lfloor\frac{W_i}{2}\rfloor}{(u_i^2 + v_i^2)}\right]^2 * X_i}; \; -\left\lfloor\frac{W_i}{2}\right\rfloor \le (u_i, v_i) \le \left\lfloor\frac{W_i}{2}\right\rfloor$$

    Output: Restored Image

End.

---

4 Experimental results and discussion

This section explicitly illustrates that our proposed algorithm can restore digital images adequately, impaired by various synthetic as well as non-synthetic periodic noise patterns. To assess the quality of restored images, our proposed *Gabor-based ANRF* algorithm is compared with other state-of-the-art approaches like MFSD1 [1], MFSD2 [2], SMF [17], WGNF [3], BNRF [22], INRF [22], AONF [27], VSNR [12], GaSF [21], AGNF [28], ASSTV [6], Sur, Grediac [36], A-contrario [35], LFDF [38], WASMF [39], ATFF [37]. These algorithms are executed using Matlab 10.0 software in Intel(R) Core(TM) i5-3210 M CPU @ 2.50 GHz processor. A few user-controlled parameters should be primarily adjusted by the

experimental study to acquire the proper results for MFSD1, MFSD2 and WGNF. Thus, best-preferred common threshold value of 10 and a window size of $9*9$ for different image-noise combinations are considered in this article. Normalizing Divider used in MFSD1 is selected as 50. $m*n$ (corrected area) are both fixed at 7 for WGNF. Parameters of Gaussian surface, i.e. A and B are fixed to 1.0 and 0.1 for WGNF and 1.0 and 0.01 for AGNF. The threshold value is considered as 25,000 for BNRF and INRF. Fixed patch size is set at best-chosen value 64 or 128 for implementing Sur, Grediac [36] and A-contrario [35] algorithms.

4.1 Performance measurement attributes

The quantitative performance metrics like Peak Signal-to-Noise Ratio (PSNR), Structural Similarity (SSIM), Edge Accuracy (εa), Edge Precision (εp) and Time Complexity (TC) in seconds are exploited in this article to assess the performance of our proposed algorithm.

4.1.1 Peak Signal-to-Noise Ratio (PSNR)

It [4] is the ratio of the maximum signal power to the power of noise that distorts the original signal. PSNR of the Denoised Image ($\hat{z}$) from the Original Image (z) is defined by,

$$PSNR = 20 \, log_{10} \frac{Max_z}{\sqrt{\frac{1}{MN} \sum_{x=0}^{M-1} \sum_{y=0}^{N-1} |z(x,y) - \hat{z}(x,y)|^2}} \, dB \tag{23}$$

4.1.2 Structural similarity (SSIM)

It is a well-matched performance metric for comparing the quality of a restored image visually and its mathematical expression are clearly outlined in [41].

$$SSIM(z, \hat{z}) = \frac{(2m_z m_{\hat{z}} + c_1)(2\sigma_{z\hat{z}} + c_2)}{(m_z^2 + m_{\hat{z}}^2 + c_1)(\sigma_z^2 + \sigma_{\hat{z}}^2 + c_2)} \tag{24}$$

Where, m_z and $m_{\hat{z}}$ refer to the mean brightness and σ_z and $\sigma_{\hat{z}}$ denotes the Standard Deviation (Std) [24] of z and $\hat{z}$ respectively. $SSIM(z, \hat{z}) = 1$, if and only if $z = \hat{z}$. More the value of SSIM approaches nearer to unity, betterment of de-noised image quality is.

4.1.3 Edge accuracy (εa) and Edge precision (εp)

The quality of a restored image can effectively be judged by the edge count, as most of the periodic noises introduce some undesired edges to the uncorrupted images. εa and εp are the two such parameters which measure the similarity between the Restored Edge-Map (ε_r) and the Original Edge Map (ε_o). Here, canny edge detection is used for finding the edge map.

$$\varepsilon a = \frac{\sum_{x=1}^{M} \sum_{y=1}^{N} [\,(T_\varepsilon) + (T_{n\varepsilon})]}{M*N} \; and \; \varepsilon p = \frac{\sum_{x=1}^{M} \sum_{y=1}^{N} [\,(T_\varepsilon)]}{\sum_{x=1}^{M} \sum_{y=1}^{N} [\,(T_\varepsilon) + (F_\varepsilon)]} \tag{25}$$

Table 1 Performance comparisons amongst different restoration filtering algorithms for a standard noise-free image Woman, impaired by single-frequency periodic noise patterns in terms of PSNR, SSIM, $\varepsilon\alpha$ and TC

Noise Pattern	Performance Metrics	MFSD1 [1]	MFSD2 [2]	SMF [17]	WGNF [3]	AONF [27]	GaSF [21]	AGNF [28]	Sur,Grediac [36]	LFDF [38]	ANRF
Impulsive-Diagonal with $A = 0.5$	PSNR	27.05	27.08	14.91	27.10	26.88	26.92	27.07	27.46	26.97	29.45
	SSIM	0.982	0.984	0.666	0.986	0.980	0.982	0.983	0.989	0.984	0.998
	$\varepsilon\alpha$	0.987	0.989	0.819	0.990	0.978	0.982	0.988	0.991	0.983	0.994
	TC (in Sec)	0.459	1.116	1.296	1.009	0.455	2.108	0.451	0.419	0.608	0.432
N_L with $A = 0.8$	PSNR	11.20	15.40	10.81	17.22	15.10	18.34	15.67	11.33	5.31	21.43
	SSIM	0.609	0.802	0.571	0.863	0.790	0.885	0.814	0.616	0.286	0.942
	$\varepsilon\alpha$	0.841	0.873	0.838	0.889	0.868	0.901	0.880	0.844	0.820	0.921
	TC (in Sec)	0.457	1.109	1.173	1.011	0.449	2.005	0.442	0.422	0.622	0.430
N_H with $A = 0.6$	PSNR	11.91	15.63	23.60	17.71	24.13	25.07	18.99	27.12	26.62	27.43
	SSIM	0.650	0.814	0.952	0.876	0.969	0.973	0.904	0.982	0.978	0.986
	$\varepsilon\alpha$	0.672	0.715	0.865	0.739	0.876	0.889	0.857	0.951	0.927	0.955
	TC (in Sec)	0.448	1.121	1.234	1.015	0.444	2.113	0.440	0.433	0.593	0.427

Table 2 Performance comparison amongst different restoration filtering algorithms in terms of PSNR, SSIM, εp and TC (in sec) for a standard noise-free image Pepper, impaired by various quasi-periodic noise patterns

Existing Filters	N_1 with $A=0.8$				N_2 with $A=0.6$				N_3 with $A=0.7$			
	PSNR	SSIM	εp	TC	PSNR	SSIM	εp	TC	PSNR	SSIM	εp	TC
MFSD1 [1]	2.62	0.137	0.116	0.468	10.48	0.496	0.623	0.459	12.92	0.635	0.123	0.471
SMF [17]	8.28	0.338	0.195	1.402	20.14	0.887	0.845	1.322	8.531	0.361	0.101	1.256
BNRF [22]	15.40	0.783	0.465	3.451	19.63	0.882	0.840	3.219	22.14	0.930	0.446	3.320
GaSF [21]	13.53	0.689	0.392	2.077	17.52	0.837	0.836	2.146	15.66	0.834	0.582	2.308
AGNF [28]	4.31	0.190	0.329	0.440	16.73	0.803	0.835	0.449	18.47	0.862	0.384	0.439
Sur, Grediac [36]	14.55	0.713	0.508	0.395	23.19	0.947	0.868	0.410	18.59	0.864	0.393	0.389
A-contrario [35]	15.23	0.737	0.475	9.157	24.26	0.956	0.877	9.342	22.52	0.937	0.459	8.798
LFDF [38]	14.50	0.708	0.431	0.697	8.450	0.385	0.799	0.725	24.42	0.961	0.595	0.638
WASMF [39]	2.05	0.122	0.104	0.607	7.403	0.326	0.778	0.581	25.06	0.962	0.615	0.632
ATFF [37]	17.32	0.821	0.485	3.112	16.14	0.782	0.810	3.373	25.47	0.969	0.632	3.650
ANRF	18.18	0.849	0.562	0.429	27.42	0.979	0.898	0.438	25.85	0.975	0.678	0.425

Where, *True Edge* (T_ε), *True Non_Edge* ($T_{n\varepsilon}$) and *Flase Edge Points* (F_ε) are given by,

$$T_\varepsilon = \begin{cases} 1, if\ \varepsilon_o(x,y) = 1\ and\ \varepsilon_r(x,y) = 1 \\ 0, \qquad\qquad\qquad\qquad\qquad otherwise \end{cases} ; T_{n\varepsilon} = \begin{cases} 1, if\ \varepsilon_o(x,y) = 0\ and\ \varepsilon_r(x,y) = 0 \\ 0, \qquad\qquad\qquad\qquad\qquad otherwise \end{cases}$$

$$and\ F_\varepsilon = \begin{cases} 1, if\ \varepsilon_o(x,y) = 0\ and\ \varepsilon_r(x,y) = 1 \\ 0, \qquad\qquad\qquad\qquad\qquad otherwise \end{cases}$$

4.2 Synthetic dataset

Likewise, other algorithms [1–3, 16, 21, 22, 27, 28, 35–39] in the literature, 10 nos. of standard noise-free natural images (Child, Woman, Lake, Lena, Cameraman, Barbara, Boats, House, Mandrill, Pepper, etc.) of size 256 ∗ 256, instigated by different periodic/quasi-periodic synthetic

Table 3 Performance comparison amongst different restoration filtering algorithms in terms of PSNR, SSIM, εp and TC (in sec) for a sample image Barbara, impaired by various quasi-periodic noise patterns

| Existing Filters	N_4 with $A=0.9$				N_5 with $A=0.5$				$N_1+N_2+N_3$ with $A=0.8$			
	PSNR	SSIM	εp	TC	PSNR	SSIM	εp	TC	PSNR	SSIM	εp	TC
MFSD2 [2]	8.352	0.392	0.141	1.120	18.22	0.842	0.271	1.075	5.314	0.242	0.148	1.084
WGNF [3]	10.93	0.539	0.251	1.096	18.65	0.874	0.386	1.009	7.961	0.372	0.185	1.019
INRF [22]	18.51	0.861	0.463	3.708	22.43	0.951	0.510	3.446	10.65	0.498	0.105	3.616
AONF [27]	11.09	0.538	0.311	0.458	18.45	0.863	0.393	0.455	10.94	0.502	0.087	0.469
AGNF [28]	11.15	0.548	0.321	0.443	19.15	0.880	0.395	0.438	3.275	0.167	0.262	0.444
Sur, Grediac [36]	16.77	0.801	0.412	0.411	21.07	0919	0.407	0.398	13.23	0.655	0.420	0.421
A-contrario [35]	17.70	0.839	0.419	8.875	21.28	0.922	0.442	9.118	15.65	0.765	0.462	9.026
LFDF [38]	18.13	0.856	0.458	0.532	24.13	0.960	0.623	0.803	5.922	0.268	0.161	0.788
WASMF [39]	4.026	0.191	0.115	0.650	24.38	0.965	0.601	0.648	2.351	0.129	0.090	0.628
ATFF [37]	19.16	0.884	0.482	3.235	24.71	0.971	0.623	3.179	13.51	0.677	0.459	3.402
ANRF	19.66	0.896	0.554	0.430	27.22	0.980	0.678	0.435	18.83	0.866	0.594	0.436
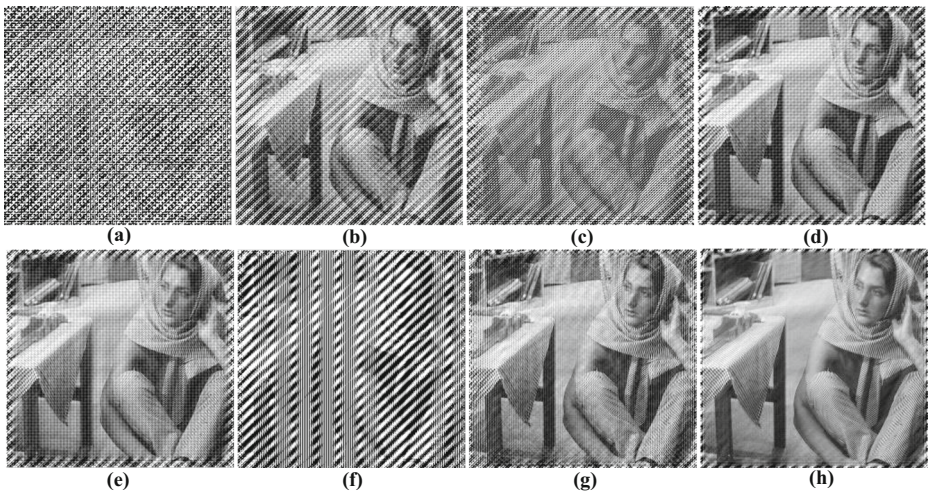
Fig. 3 **a** Standard noise-free image Barbara, contaminated by combined noise $N_1 + N_2 + N_3$ with $A = 0.7$; denoised images with **b** WGNF; **c** AGNF; **d** Sur, Grediac; **e** A-contrario; **f** WASMF; **g** ATFF; **h** ANRF

sinusoidal noisy patterns are experimentally analysed in our article. Amongst them, Lena, Woman, Pepper, and Barbara are presented here. In Table 1, low and high-frequency periodic noise structures with Noise Strength (A) are considered as the noise source as in Eq. (26a) and (26b):

$$N_L(x,y) = A^* \left[sin\left(\frac{x}{3} + \frac{y}{5}\right) \right] \tag{26a}$$

$$N_H(x,y) = A^* \left[sin(x+y) \right] \tag{26b}$$

Table 1 explicitly exemplifies that our proposed *Gabor-based ANRF* algorithm outperforms all other existing algorithms for a sample image Woman of size (256 ∗ 256) with proficient TC for impulsive-diagonal, N_L and N_H periodic noise patterns in terms of PSNR, SSIM and εa in a fully adaptive way.

The suppression of multi-frequency periodic noises from images, generated by sinusoidal functions is a challenging problem in comparison to any single-frequency periodic noise pattern where usually almost all compared restoration algorithms can perform well. Therefore, in this article, five artificially generated multi-frequency periodic/quasi-periodic noise models
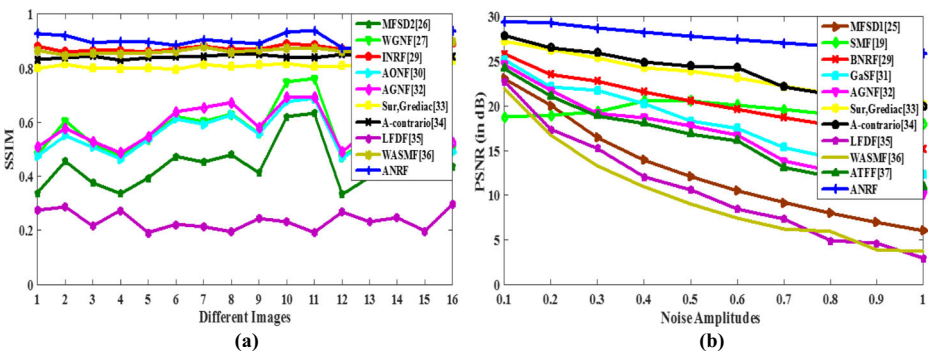
Fig. 4 Performance comparisons of 16 different images, contaminated by N_4 with $A = 0.9$ w. r. t. **a** SSIM; Plot of **b** PSNR versus varying noise amplitudes (A) for N_2 as in Eq. (27b)
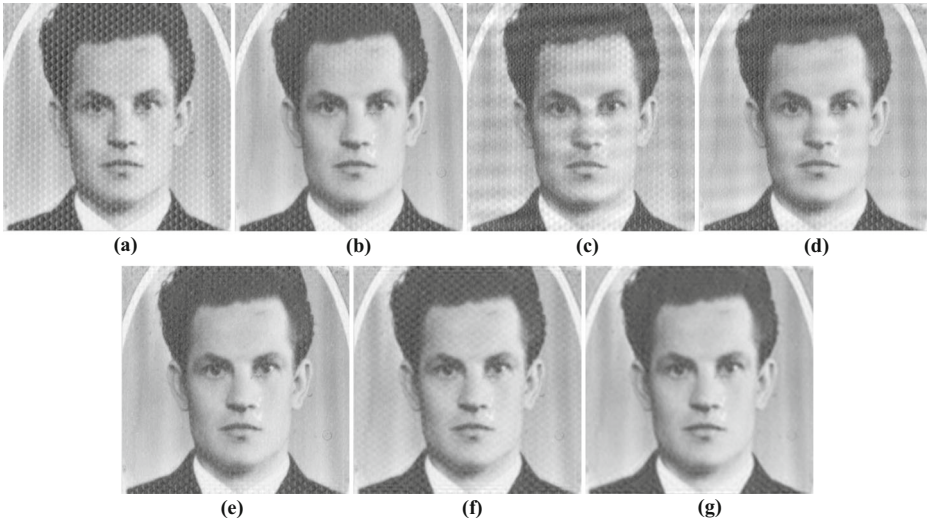
Fig. 5 **a** Non-synthetically corrupted image Man; de-noised images with **b** WGNF; **c** GaSF; **d** AGNF; **e** A-contrario; **f** WASMF; **g** ANRF

$(N_1, N_2, N_3, N_4, N_5)$ are considered for testing the restoration capability of different algorithms.

$$N_1(x,y) = A*[sin(2x+2y) + sin(0.5x+0.5y) + sin(3x) + sin(4y)] \quad (27a)$$

$$N_2(x,y) = A*[3.25\ sin(x) + 8.65\ sin(y)] \quad (27b)$$

$$N_3(x,y) = A*[sin(8y) + sin(8x) + sin(5.25x+5.25y) + sin(x+5.25y)] \quad (27c)$$

$$N_4(x,y) = A*[sin(0.5x{-}0.5y) + sin(1.5x{-}1.5y) + sin(2.5x{-}2.5y)] \quad (27d)$$

$$N_5(x,y) = A*[sin(1.1x+1.1y) + sin(1.5x) + sin(1.5y) + sin(1.1x{-}1.1y)] \quad (27e)$$
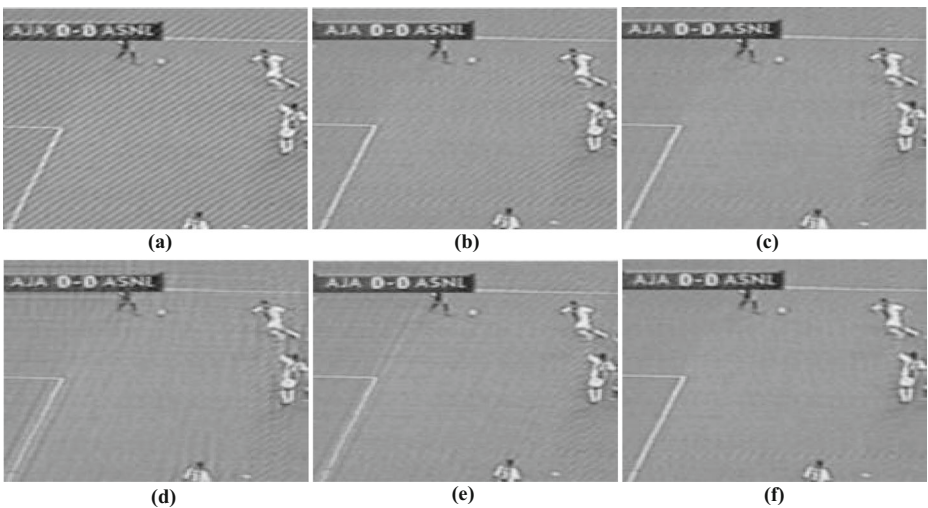
Fig. 6 **a** Close-up view of non-synthetically corrupted image Television; de-noised images with **b** WGNF; **c** Sur, Grediac; **d** WASMF; **e** ATFF; **f** ANRF
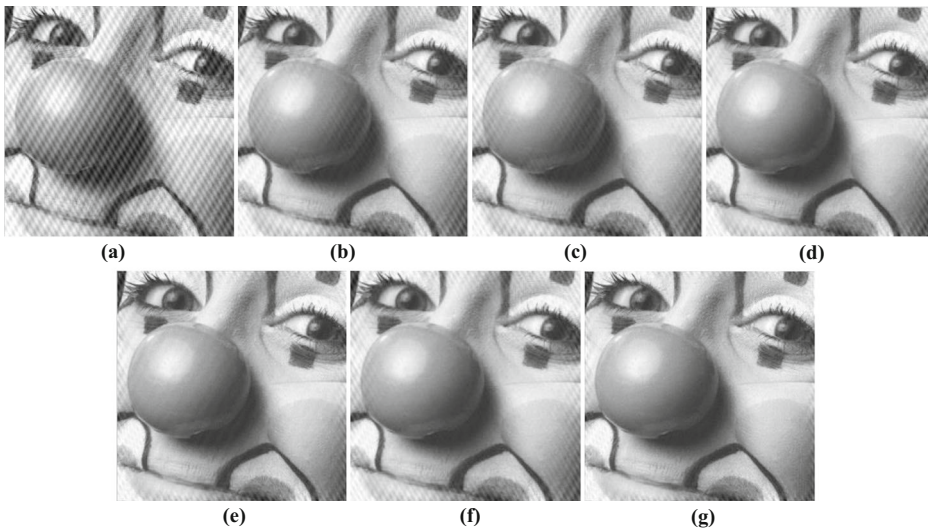
Fig. 7 **a** Non-synthetically corrupted image Clown; de-noised images with **b** WGNF; **c** GaSF; **d** AGNF; **e** Sur, Grediac; **f** WASMF; **g** ANRF

Tables 2 and 3 and Fig. 3 clearly illustrate that our proposed *Gabor-based ANRF* algorithm is always able to attain higher performances both quantitative and qualitatively than other competing algorithms while restoring digital images for various synthetically generated quasi-periodic noise structures with considerable TC.

In Fig. 4a, it is graphically depicted that our proposed *Gabor-based ANRF* algorithm outshines all other existing algorithms for 16 numbers of synthetically corrupted images in terms of SSIM. For our algorithm, SSIM always approaches towards unity. From Fig. 4b, it is clear that the performance of our proposed algorithm is the best among other existing algorithms in terms of PSNR for a sample image Pepper with varying noise amplitudes ($A = 0.1$ *to* 1).
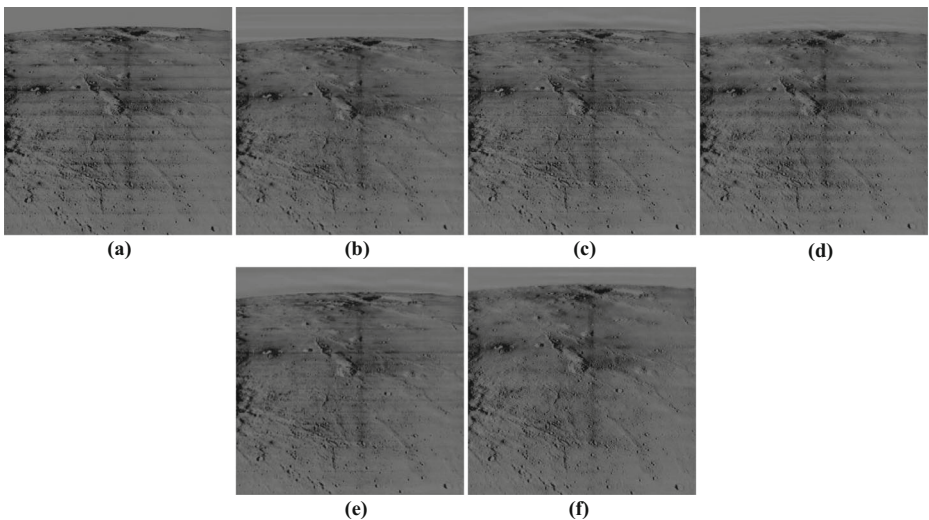
Fig. 8 **a** Close-up view of astronomical mission image Lunar Orbiter 2, impaired by non-synthetic periodic noise pattern; de-noised images with **b** WGNF; **c** AONF; **d** Sur, Grediac; **e** LFDF; **f** ANRF
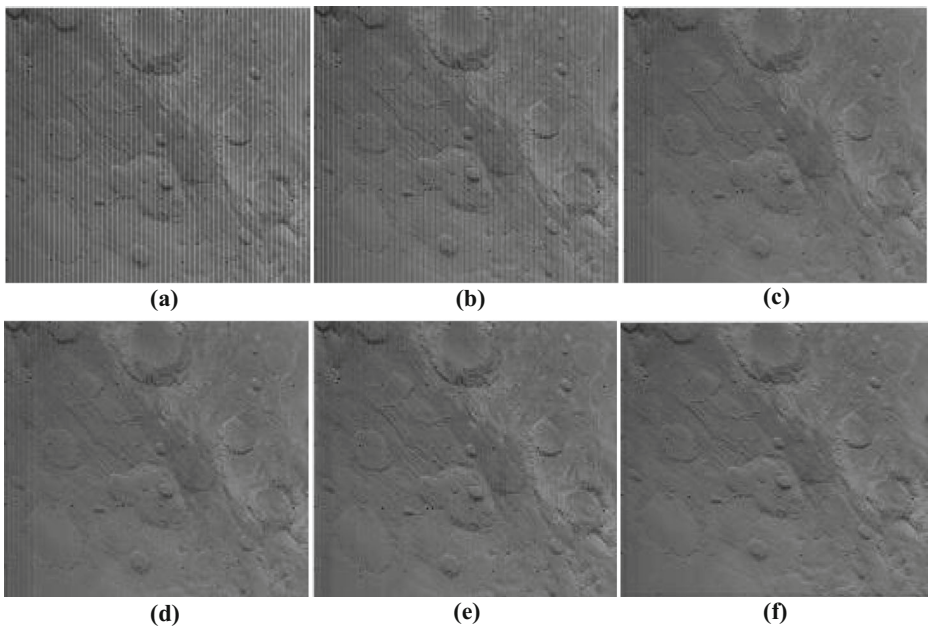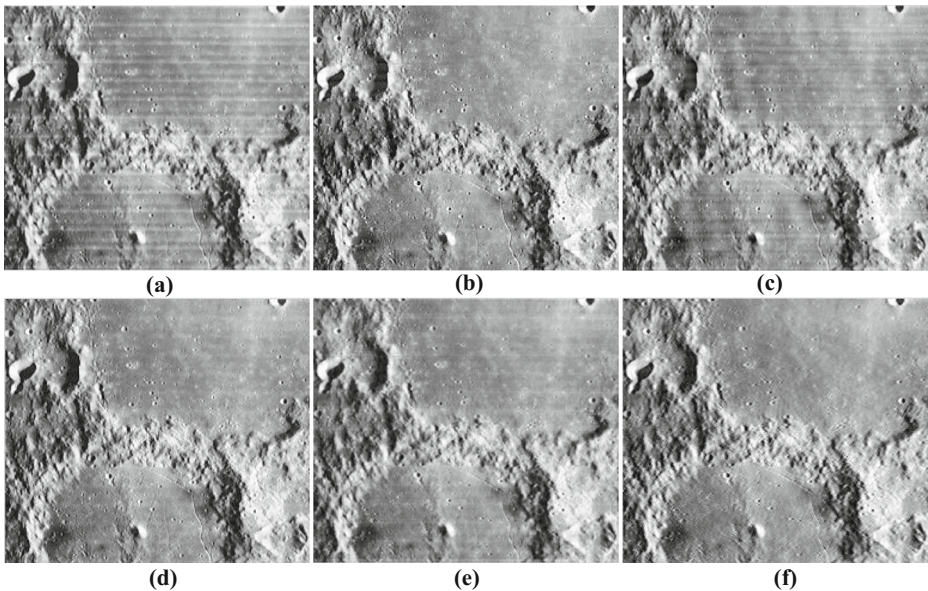
Fig. 9 **a** Close-up view of astronomical mission image Vicking Orbiter, impaired by non-synthetic vertical periodic striping noise pattern; de-noised images with **b** AGNF; **c** Sur, Grediac; **d** ASSTV; **e** WASMF; **f** ANRF

4.3 Non-synthetic dataset in real-time imaging applications

A series of non-synthetic dataset from a wide range of realistic scenarios are now presented as an example to demonstrate the restoration capability of our proposed approach. As the original image is

Fig. 10 **a** Close-up view of astronomical mission image Lunar Orbiter 4, impaired by non-synthetic horizontal striping noise pattern; de-noised images with **b** VSNR; **c** AGNF; **d** ASSTV; **e** A-Contrario; **f** ANRF
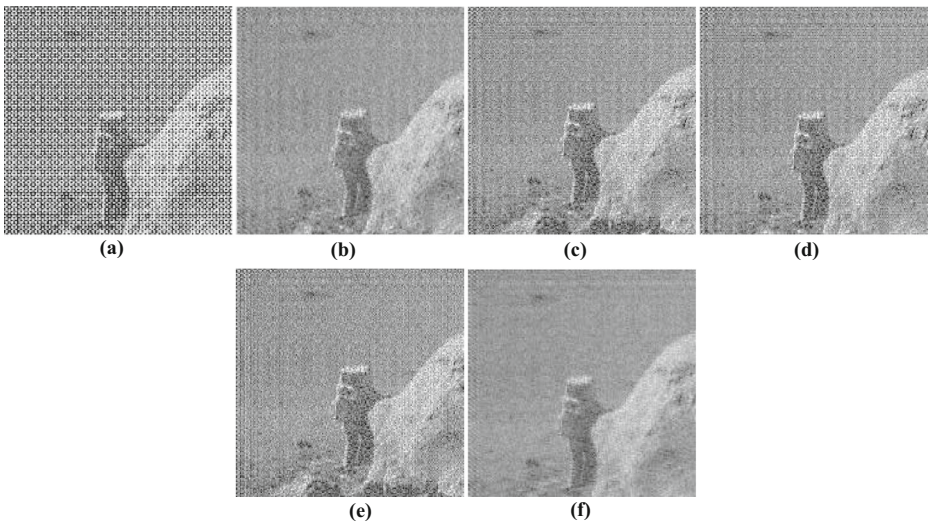
Fig. 11 **a** Close-up view of non-synthetically corrupted image Apollo, impaired by periodic noise pattern; restored images with **b** A-contrario; **c** LFDF; **d** WASMF; **e** ATFF; **f** ANRF

not within the reach, the quantitative performance evaluation cannot be computed for non-synthetic dataset. 25 numbers of non-synthetically corrupted images from various fields are examined by us as a benchmark. Here, a few of them are presented from Figs. 5, 6 and 7, thereby proving that our algorithm outperforms other most recent state-of-the-art algorithms for a few non-synthetically corrupted images like Man, Television and Clown in realistic situations.

The visual inspection of Figs. 8, 9, 10 and 11 establishes the superiority of our proposed *Gabor-based ANRF* algorithm as it produces better-restored images in comparison to recent similar kind of algorithms for various non-synthetically corrupted images taken from the
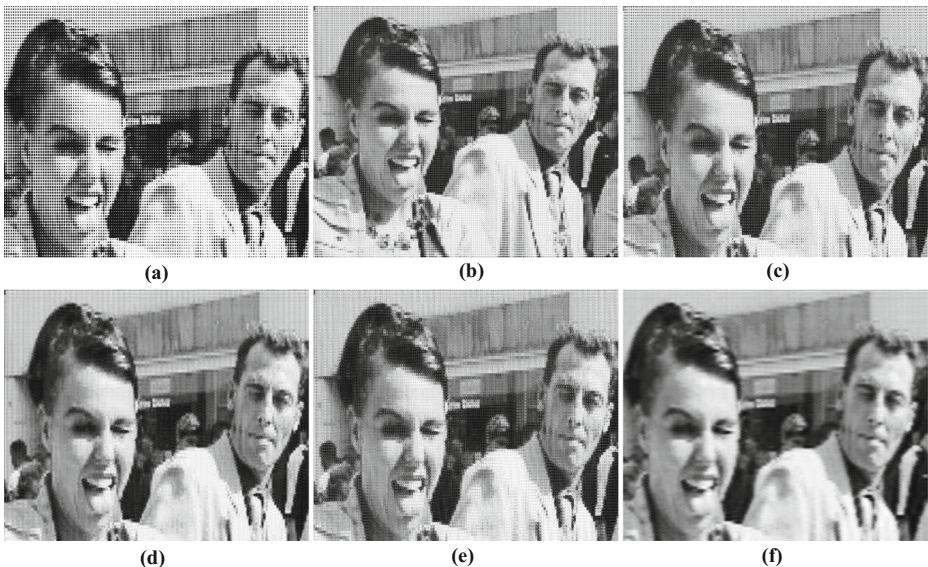

Fig. 12 **a** Close-up view of naturally corrupted halftone image Lady-Man, de-noised images with **b** WGNF; **c** AGNF; **d** Sur, Grediac; **e** LFDF; **f** ANRF
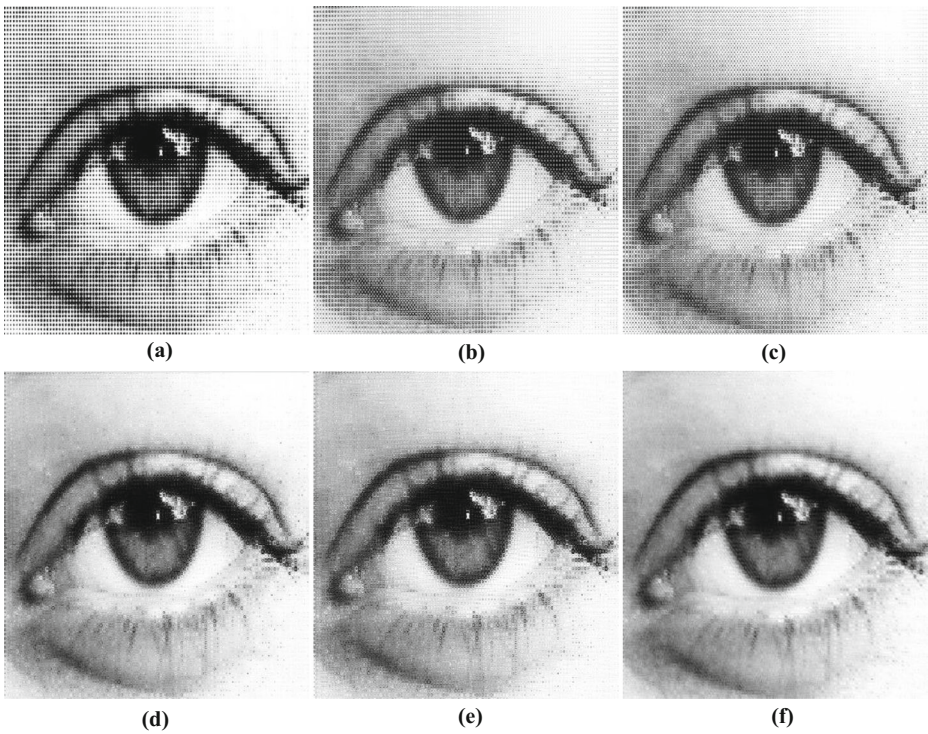
Fig. 13 **a** Close-up view of naturally corrupted halftone image Halftone-eye, de-noised images with **b** WGNF; **c** AONF; **d** Sur, Grediac; **e** LFDF; **f** ANRF
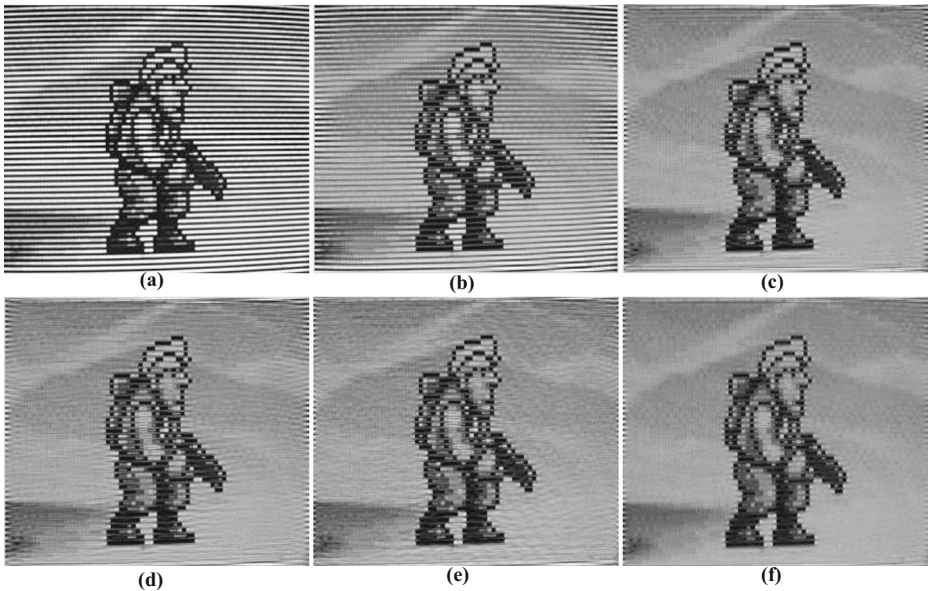

Fig. 14 **a** Close-up view of Scanline image, impaired by non-synthetic periodic noise pattern; de-noised images with **b** AONF; **c** A-Contrario; **d** WASMF; **e** ATFF; **f** ANRF
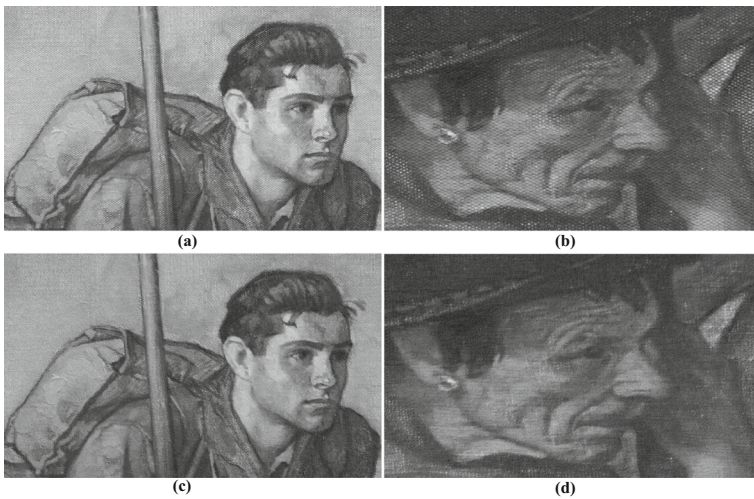
Fig. 15 Non-synthetically corrupted images: close-up view of **a** Rockwell - Carry On - 002; **b** Rockwell - Our Heritage - 002; Outputs using our proposed ANRF approach **c** de-noised Rockwell - Carry On - 002 image; **d** de-noised Rockwell - Our Heritage - 002 image

astronomical mission (orbiter/landing) image gallery, conducted by *American space agency* (NASA: National Aeronautics and Space Administration).

Quasi-periodic structures can also be generated through a certain specific types of reprographic methods such as halftone printing (generates a continuous toned gradient-like imagery through the use of varying dots either in size/in space) and visible raster scan line in Cathode Ray Tube (CRT) monitors. Here, the performance of our *Gabor-based ANRF* algorithm for a few non-synthetically corrupted images (Figs. 12, 13 and 14), produced by any reprographic technique is evaluated with few other competent algorithms.
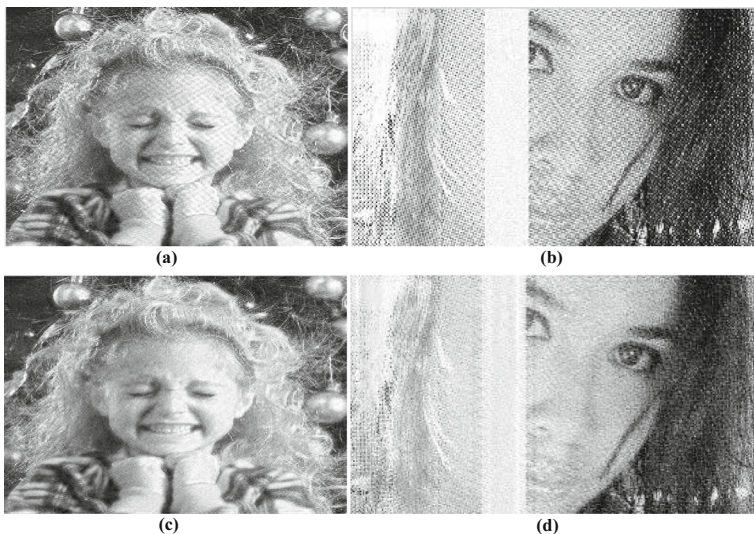

Fig. 16 Real images, contaminated by non-synthetic moiré pattern: **a** Moiré 1; **b** Moiré 2; Outputs using our ANRF algorithm **c** de-noised image of Moiré 1; **d** de-noised image of Moiré 2

Applicability of our algorithm is also investigated for removing canvas contamination in digital images of painting artwork (Fig. 15) where periodic plane of the support weave can be regarded as noise.

Figure 16 depicts the qualitative performance of the restored images using our proposed algorithm for two natural images, corrupted with a special kind of non-synthetic periodic pattern i.e. *Moiré* in case of realistic circumstances.

5 Conclusion

An ingenious spectral domain de-noising algorithm for periodically corrupted images of various real-time imagery systems has been demonstrated in this paper. A few initial steps of our proposed algorithm illustrate the preservation mechanism of the most informative LFR region followed by the contrast enhancement of LFR preserved image spectrum by using Gabor transform to highlight all the noisy regions outstandingly. Then, those noisy regions are properly detected using our proposed adaptive exponential thresholding procedure. After that, those noisy components are filtered out using our proposed adaptive notch-reject filter with an automated control of filtering profile in accordance with the radial span of different kinds of noise spectrum profiles. Experimental results for both synthetic and non-synthetically corrupted images proved that our proposed Gabor-based ANRF algorithm outperforms other popular exiting algorithms both qualitatively and quantitatively. The time consumption of our algorithm is also found to be effective while comparing with the literature.

Publisher's Note Springer Nature remains neutral with regard to jurisdictional claims in published maps and institutional affiliations.

References

1. Aizenberg I, Butakoff C (2002) Non-linear frequency domain filter for quasi periodic noise removal. In: Proceeding of International TICSP Workshop on Spectra Methods and Multi-rate Signal Processing. TICSP Series, 17, pp 147–153
2. Aizenberg I, Butakoff C (2002) Frequency domain median-like filter for periodic and quasi-periodic noise removal. SPIE Proceedings of the Image Processing 4667:181–191
3. Aizenberg I, Butakoff C (2008) A windowed Gaussian notch filter for quasi-periodic noise removal. Image Vis Comput 26(10):1347–1353
4. Al-Najjar YA, Soong DC (2012) Comparison of image quality assessment: PSNR, HVS, SSIM, UIQI. International Journal of Scientific & Engineering Research 3(8):1–5 ISSN 2229-5518
5. Castelli V, Bergman LD (2002) Image databases: search and retrieval of digital imagery. Wiley, New York
6. Chang Y et al (2015) Anisotropic spectral-spatial total variation model for multispectral remote sensing image destriping. IEEE Trans Image Process 24(6):1852–1866
7. Chang-Yanab C, Ji-Xiana Z, Zheng-Juna L (2008) Study on methods of noise reduction in a striped image. Int Arch Photogramm Remote Sens Spat Inf Sci XXXVII:B6b
8. Cornelis B et al (2012) Digital canvas removal in paintings. Signal Process 92(4):1166–1171
9. Daugman JG (1980) Two-dimensional spectral analysis of cortical receptive field profiles. Vis Res 20(10):847–856
10. Daugman JG (1985) Uncertainty relation for resolution in space, spatial frequency, and orientation optimized by two-dimensional visual cortical filters. JOSA A 2(7):1160–1169
11. Drigger R, Cox P, Edwards T (1999) Introduction to infrared and electro-optical system. Artech House, Norwood
12. Fehrenbach J, Weiss P, Lorenzo C (2012) Variational algorithms to remove stationary noise: applications to microscopy imaging. IEEE Trans Image Process 21(10):4420–4430

13. Feuerstein D, Kim HP, Martyn GB (2009) Practical methods for noise removal: applications to spikes, nonstationary quasi-periodic noise, and baseline drift. Anal Chem 81(12):4987–4994
14. Gonzalez RC, Woods RE (2007) Digital image processing, 3rd edn. Prentice Hall, Upper Saddle River, New Jersey
15. Guttman N, Julesz B (1963) Lower limits of auditory periodicity analysis. J Acoust Soc Am 35(4):610–610
16. Hudhud GAA, Turner MJ (2005) Digital removal of power frequency artifacts using a Fourier space median filter. IEEE Signal Processing Letters 12(8):573–576
17. Ji Z et al (2006) Simple and efficient soft morphological filter in periodic noise reduction. In: TENCON 2006–2006 IEEE Region 10 Conference, IEEE, pp. 1–4
18. Ji TY et al (2007) Optimal soft morphological filter for periodic noise removal using a particle swarm optimiser with passive congregation. Signal Process 87(11):2799–2809
19. Jing W, Liu DC (2010) 2-D FFT for periodic noise removal on strain image. International conference on bioinformatics and biomedical engineering, Chengdu, China
20. Kelcey J, Arko L (2012) Sensor correction of a 6-band multispectral imaging sensor for UAV remote sensing. Remote Sens 4:1462–1493
21. Ketenci S, Gangal A (2012) Design of Gaussian star filter for reduction of periodic noise and quasi-periodic noise in gray level images. In: Innovations in Intelligent Systems and Applications (INISTA), IEEE, pp. 1–5. https://doi.org/10.1109/INISTA.2012.6246937
22. Konstantinidis AC et al (2010) Optical characterisation of a CMOS active pixel sensor using periodic noise reduction techniques. Nuclear Instruments and Methods in Physics Research Section A: Accelerators, Spectrometers, Detectors and Associated Equipment 620(2):549–556
23. Koukou, V et al (2015) Dual energy method for breast imaging: a simulation study. Computational and Mathematical Methods in Medicine 1–8
24. Kumar V, Gupta P (2012) Importance of statistical measures in digital image processing. International Journal of Emerging Technology and Advanced Engineering 2(8), ISSN 2250-2459
25. Marques O (2011) Practical image and video processing using MATLAB. Wiley, Hoboken, New Jersey
26. Milanfar P (2013) A tour of modern image filtering: new insights and methods, both practical and theoretical. IEEE Signal Process Mag 30:106–128
27. Moallem P, Behnampour M (2010) Adaptive Optimum Notch Filter for Periodic Noise Reduction in Digital Images. Amirkabir International Journal of Electrical & Electronics Engineering 42(1):1–7
28. Moallem P et al (2015) A novel adaptive Gaussian restoration filter for reducing periodic noises in digital image. SIViP 9(5):1179–1191
29. Rindfleisch TC et al (1971) Digital processing of the mariner 6 and 7 pictures. J Geophys Res 76(2):394–417
30. Saravanakumar S (2013) Removal of moiré pattern noise in images using median and gaussian filter. International Journal of Science, Engineering and Technology Research 2(2):380–385
31. Schowengerdt R (2006) Remote sensing: models and methods for image processing. Academic, Orlando
32. Smith RD (2012) Digital transmission systems, 3rd edn. Springer Science & Business Media, Heidelberg
33. Song M, Tao D, Chen C, Bu J, Yang Y (2013) Color-to-gray based on chance of happening preservation. Neurocomputing 119:222–231
34. Sugiura Y, Kawamura A, Aikawa N (2013) A comb filter with adaptive notch bandwidth for periodic noise reduction. In: Information, Communications and Signal Processing (ICICS) 2013 9th International Conference on IEEE, pp 1–4
35. Sur F (2015) An a-contrario approach to quasi-periodic noise removal. In: International Conference on Image Processing (ICIP), IEEE, pp. 3841–3845. https://doi.org/10.1109/ICIP.2015.7351524
36. Sur F, Grédiac M (2015) Automated removal of quasiperiodic noise using frequency domain statistics. Journal of Electronic Imaging 24(1):013003_1–013003_19
37. Varghese J Adaptive threshold based frequency domain filter for periodic noise reduction. AEU Int J Electron Commun 70(12):1692–1701
38. Varghese J et al (2016) Laplacian-based frequency domain filter for the restoration of digital images corrupted by periodic noise. Can J Electr Comput Eng 39(2):82–91
39. Varghese J et al (2016) Fourier transform-based windowed adaptive switching minimum filter for reducing periodic noise from digital images. IET Image Process 10(9):646–656
40. Vaseghi VS (2013) Advanced signal processing and digital noise reduction, 3rd edn. Wiley, Hoboken, New Jersey
41. Wang Z et al (2004) Image quality assessment: from error visibility to structural similarity. IEEE Trans Image Process 13(4):600–612
42. Wang Y, Wang Z, Tao D, Zhuo S, Xu X, Pu S, Song M (2017) All Focus: patch-based video out-of-focus blur reconstruction. IEEE Transactions on Circuits and Systems for Video Technology 27(9):1895–1908

Mrs. D. Chakraborty is pursuing Ph.D. in the Dept. of Electronics and Telecommunication Engineering from IIEST, Shibpur, India. She has completed her M.E. with specialization in Digital System & Instrumentation from IIEST, Shibpur, India. She has obtained B. Tech from Heritage Institute of Technology, Kolkata, India in Electronics & Communication Engineering. Her research interest includes Design of spreading codes for CDMA application, Digital Signal, Image Processing and VLSI design.

Mr. M. K. Tarafder is pursuing Ph.D. in the Dept. of Electronics and Telecommunication Engineering from IIEST, Shibpur, India. He has completed her M.E. with specialization in Communication Engineering and Signal processing from IIEST, Shibpur, India. He has obtained B.Tech in Electronics and Communication Engineering from RCC Institute of Information Technology, Kolkata, India. His research interest includes Digital Image Processing and VLSI design, Recognition.

Prof. A. Banerjee is presently working as an Associate Professor in the Department of Electronics & Telecommunication Engineering at IIEST, Shibpur, India. He has obtained B.E. on 1994 from Bengal Engineering College, Shibpur, Calcutta University and M. Tech. from IIT, Kharagpur in Electronics and Electrical Communication Engineering with specialization in Integrated Circuits and Systems Engineering on 1999. He has completed his Ph.D. from IIT, Kharagpur on 2013 successfully. His research area includes Digital Signal/Image Processing, VLSI Architectures for Communication and Biomedical Engineering, CORDIC based DSP architectures etc. He has authored a number of Journal and Conference papers of International repute.

Prof. S. R. Bhadra Chaudhuri is presently working as Professor in the Department of Electronics and Telecommunication Engineering at IIEST, Shibpur, India. He has obtained his B.E. in Electronics and Telecommunication Engineering, M.E., M. B. A. from Calcutta University, India. He has achieved his Ph.D. degree from Jadavpur University. His research area includes Microstrip antenna and circuits, Wireless / Mobile Communication & Network, Information & Network Security, Digital System Design, Human Resource & Marketing Management, Digital Signal/Image Processing. He has authored a lot of Journal and Conference papers of International repute. He has received Patent and reviewed lots of reputed journals as reviewer.